

# In Situ Growth of Carbon Dots on Acid-Modified Nanoclay for Advanced MoS<sub>2</sub> Composite-Based Asymmetric Supercapacitor

Khusboo Kumari, Arif Ali, Sourav Acharya, Chandan Kumar Maity,\* and Ganesh Chandra Nayak\*

This study presents an innovative strategy for utilizing passive cigarette smoke aerosol, a common pollutant, to prepare a sustainable supercapacitor cathode. The cathode system is developed with *in situ* growth of carbon dots from cigarette smoke aerosol on the acid modified nanoclay (ANc), which reduces the internal resistance of layered silicates. The modified nanoclay is subsequently combined with pseudocapacitive layered MoS<sub>2</sub> to enhance the electrochemical performance by redox reaction during charging and discharging cycles. To achieve optimum conductivity and specific capacitance (Sp.Cp.), both carbon dots and MoS<sub>2</sub> loading are varied and corresponding Sp.Cp. is calculated in the three electrode and asymmetric device configuration, respectively. The successful formation of the carbon dot modified ANc based MoS<sub>2</sub> composite is confirmed through a combination

of structural, morphological, and spectroscopic characterization techniques. Asymmetric supercapacitor devices are fabricated using the synthesized nanocomposite as the positive and graphite as the negative electrode in 1 M TEABF<sub>4</sub> /DMSO electrolyte. Among acid modified nanocomposites, the device containing double the quantity of MoS<sub>2</sub> shows a maximum Sp.Cp. of 119.7 F g<sup>-1</sup> with 26.7 Wh kg<sup>-1</sup> energy density and 500 W kg<sup>-1</sup> power density at 1 A g<sup>-1</sup> current density. Furthermore, the optimized electrode is able to illuminate red and disco LED lights, highlighting its potential application in sustainable energy storage systems. This work presents a novel approach for utilizing cigarette smoke aerosol into high performance supercapacitor electrode materials.

## 1. Introduction

Current global data indicate that energy consumption and environmental pollution are rising daily, which have catalyzed the growth of clean, renewable energy sources, including wind, solar, and tidal energy. Nevertheless, the intermittent and seasonal nature of these energy sources makes it challenging for them to produce power on demand.<sup>[1]</sup> This has led to a great deal of focus on electrochemical energy storage technologies, which include supercapacitors (SCs), rechargeable batteries, and fuel cells.<sup>[2,3]</sup> Among these, SCs have advantages owing to their lucrative features like long cyclic stability, high power density, average energy density, low cost, and fast charging and discharging rates.<sup>[4–7]</sup> The performance of SC is largely influenced by the

material's surface area, structural stability, redox active sites, porosity, electrical conductivity, and layer spacing for fast ion diffusion. Since layered materials naturally possess these qualities, they are very appealing for use as SC electrodes. Because of this, researchers are interested in the exploration of more layered nanomaterials beyond graphene, such as layered nanoclay,<sup>[8–11]</sup> bismuthene,<sup>[12]</sup> phosphorene,<sup>[13]</sup> transition metal dichalcogenides,<sup>[14–16]</sup> and 2D graphene analogs.<sup>[17]</sup>

In contrast to other layered nanomaterials, natural nanoclay is abundant, has huge specific surface area, is of lower cost, and has layered structure which adds to the porosity and results in faster ion diffusion in and out of the structure. Since it is incompatible with organic solvents due to its hydrophilic nature, it is modified using methyl tallow bis(2-hydroxyethyl) quaternary ammonium salt, an organic surfactant. The surface of organically modified MMT is negatively charged because Al<sup>3+</sup> frequently replaces Si<sup>4+</sup> in the structure, and Mg<sup>2+</sup>, Fe<sup>2+</sup>, and other low valent cations can easily substitute Al<sup>3+</sup>, which further helps in efficient charge storage via intercalation. Soni et al.<sup>[18]</sup> reported the different types of modification of natural nanoclay using mineral and organic acids to enhance the physical and chemical properties. Chikkatti et al. reported poly(lactic acid)/halloysite nanoclay film having a Sp.Cp. of 197.7 mF g<sup>-1</sup> at a current density of 0.45 mA g<sup>-1</sup> with 10.8 mWh kg<sup>-1</sup> energy density and 549 mW kg<sup>-1</sup> power density.<sup>[19]</sup> Although nanoclay has high surface area due to its layered structure, it suffers from inherently low electronic conductivity, which can be addressed by incorporating conductive

K. Kumari, A. Ali, S. Acharya, G. C. Nayak  
Department of Chemistry and Chemical Biology

Indian Institute of Technology (ISM)  
Dhanbad, Jharkhand 826004, India  
E-mail: gcnayak@iitism.ac.in

C. K. Maity  
Department of Chemistry  
Gachon University  
1342 Seongnam-daero, Sujeong-gu, Seongnam-si 13120, Gyeonggi-do,  
Republic of Korea  
E-mail: ckmkorea@gachon.ac.kr

 Supporting information for this article is available on the WWW under <https://doi.org/10.1002/batt.202500429>

carbonaceous materials. Timakwe et al. reported how the incorporation of carbonaceous materials can improve the electronic conductivity of nanoclay.<sup>[20]</sup> Inayat et al. reported hydrothermally derived carbon quantum dots (CQDs) from spent tea leaves, which delivered a Sp.Cp. of  $144.4 \text{ F g}^{-1}$  at  $20 \text{ A g}^{-1}$  current density.<sup>[21]</sup> Hoang et al. synthesized electrode material using carbon dots (CDs) from Zucchini leaves and reduced graphene oxide (rGO) via a hydrothermal approach, achieving a Sp.Cp. of  $374 \text{ F g}^{-1}$  at  $2 \text{ mV s}^{-1}$  scan rate utilising three electrode configuration with 71.7% capacitance retention.<sup>[22]</sup> In this work, hazardous cigarette smoke having different  $\pi$  conjugated organic components has been used to hydrothermally synthesize CDs on acid modified nanoclay surface. CDs are commonly regarded as materials for supporting electrodes due to their ability to enhance ionic mobility, facilitate electron transport, and increase the effective interaction area between the electrode and electrolyte.<sup>[23,24]</sup>

A significant obstacle that SCs face is their relatively low energy density. To get around this restriction, it is necessary to combine an electric double layer capacitor (EDLC) and pseudocapacitor type of materials to create hybrid SC electrodes. Here, EDLC type CDs deposited over acid modified nanoclay (ANc) were integrated with pseudocapacitive type MoS<sub>2</sub> to improve the overall SC performance. The selection of MoS<sub>2</sub> for this work is preferred because the layers of MoS<sub>2</sub> facilitate intercalation and redox activity along with their high tolerance towards structural integrity during charge/discharge cycles.<sup>[25]</sup> Here, nanoclay layers provide porosity and function as ion transport channels and as spacers to stabilize MoS<sub>2</sub> exfoliation. Due to their different architectures, the two primary phases of MoS<sub>2</sub> are semiconducting- (2H phase) and metallic- (1T phase) in nature.<sup>[26,27]</sup> The metallic phase provides conductivity and

electrochemical activity whereas semiconducting phase offers structural stability.<sup>[28,29]</sup> Kumar et al. reported a symmetric SC (MSWT//MSWT) which demonstrated an exceptional performance, achieving a Sp.Cp. of  $84 \text{ F g}^{-1}$  at  $0.25 \text{ A g}^{-1}$ .<sup>[30]</sup> As per literature, CDs and MoS<sub>2</sub> based composites have been reported for SC application. Maity et al. reported Zn-MoS<sub>2</sub>/CDs@BN based flexible SC device having a Sp.Cp. of  $89 \text{ F g}^{-1}$  at  $4 \text{ A g}^{-1}$  current density.<sup>[31]</sup> Abuelela et al. reported biochar derived activated carbon from sugar beet molasses hydrothermally and modified with MoS<sub>2</sub> (AC-MoS<sub>2</sub>) for SC with a Sp.Cp. of  $114.2 \text{ F g}^{-1}$  at a current density of  $1 \text{ A g}^{-1}$ .<sup>[32]</sup>

This study presents an integrated approach to alleviate the energy and environmental issues. Cigarette smoke not only harms active smokers but also poses serious health risks to passive smokers. The smoke pollutes the air, while its residue contaminates soil and water. Here, the ingenious combination of the each material mitigates the drawbacks of one another. To improve the electronic conductivity of nanoclay, it is modified by depositing CDs which in addition to improving the conductivity will increase the surface area for better electrode electrolyte interaction. For the best electrochemical performance, the amount of dispersion used to modify the ANc sheets with respect to the dispersion of cigarette extract was optimized by their charge storage capacity in three electrode analysis. These composites were then combined with MoS<sub>2</sub> in various ratios to form hybrid materials, which was further optimized concerning their charge storage capacitive performances in an asymmetric device as a cathode using an organic electrolyte 1 M TEABF<sub>4</sub>/DMSO in 0–1.6 V potential window. Figure 1 shows the graphical illustration for the synthesis of MoS<sub>2</sub> based CDs deposited acid-modified nanoclay electrode materials.

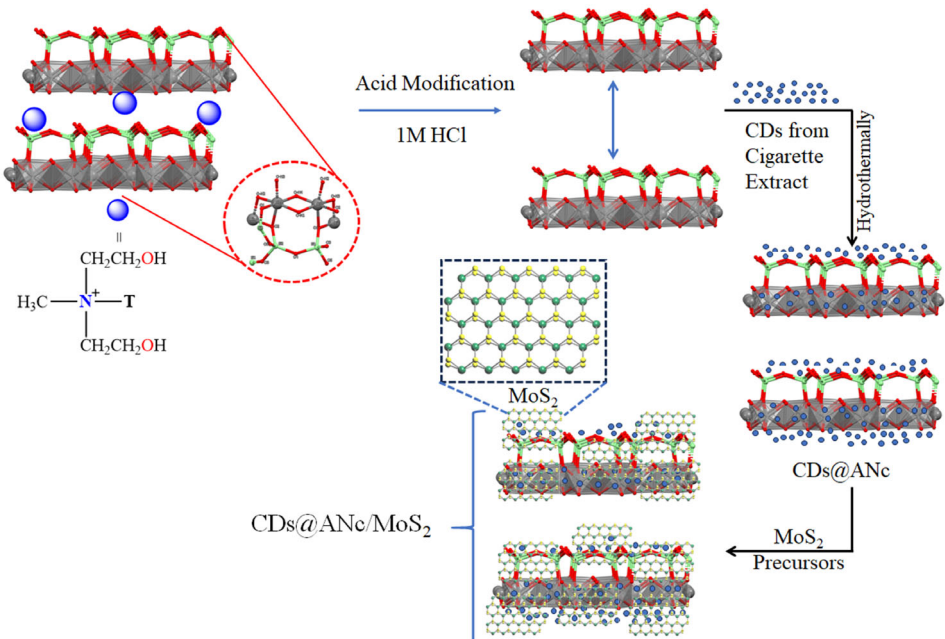


Figure 1. Schematic illustration of MoS<sub>2</sub>-based CDs@ANc composites.

## 2. Experimental Section

All analytical grade chemicals were utilized without any additional purifications in order to synthesize electrode materials. Section S1, Supporting Information, covers the details of each material used for this work.

### 2.1. Synthesis of ANc

For synthesis of ANc, initially, 1 g nanoclay (Nc) was added to 50 mL of 1 M HCl in a beaker and sonicated until proper dispersion was attained. It was then left under stirring overnight at 60 °C. The cream colored product was obtained by centrifugation and washed with deionized (DI) water until neutralized and kept for drying at 60 °C in an oven. The product obtained was named as ANc.

### 2.2. Synthesis of Cigarette Extract

Initially, cigarette smoke aerosol was captured by a specially designed glass apparatus as shown in Figure S1a, Supporting Information. The apparatus was connected with a vacuum pump through a silica trap to arrest the excess vapors as shown in Figure S1b, Supporting Information. The whole vapors were absorbed in DI water, and this extract was used for the synthesis of CDs (Supporting video V1, Supporting Information).

### 2.3. Synthesis of CD-Deposited ANc (CDs@ANc)

Initially, 50 mg ANc was mixed with 15 mL of cigarette extract and the volume of the above mixture was adjusted with DI water up to 30 mL, sonicated until uniform dispersion was attained and left under stirring overnight. The above solution was transferred to a 50 mL Teflon lined stainless steel autoclave and kept at 200 °C for 12 h. Post hydrothermal treatment light brown color filtrate was collected, and the residue was washed with DI water. The product was dehydrated at 60 °C and named as CDs@ANc. In addition, different compositions of CDs@ANc (CDs@ANc-2.5, CDs@ANc-5, CDs@ANc-10, and CDs@ANc-30) were synthesized using 2.5, 5, 10, and 30 mL of cigarette extract. Table S1, Supporting Information, summarizes the amount of cigarette extract and ANc used to fabricate different CDs@ANc composites (Figure 1).

### 2.4. Synthesis of Molybdenum Disulfide-Based CDs@ANc Composite (CDs@ANc/MoS<sub>2</sub>)

To synthesize the molybdenum disulfide ,modified CDs@ANc, initially CDs@ANc (30 mg) was dispersed in DI water (20 mL) and ultrasonicated until effective dispersion was attained. To the aforesaid homogenous dispersion, 0.15 g sodium molybdate dihydrate was added under constant stirring followed by 0.30 g thioacetamide to make a homogeneous solution and left under stirring for 3 h. To a 50 mL Teflon lined stainless steel autoclave, the solution was transferred and treated for 24 h at 200 °C. After hydrothermal treatment, the product was washed with DI water

**Table 1.** Amount of reagents employed for the synthesis of different CDs@ANc/MoS<sub>2</sub> samples.

Sample name	CDs@ANc [mg]	Sodium molybdate dihydrate [g]	Thioacetamide [g]
CDs@ANc/MoS <sub>2</sub> 11	30	0.075	0.15
CDs@ANc/MoS <sub>2</sub> 12	30	0.15	0.30
CDs@ANc/MoS <sub>2</sub> 21	60	0.075	0.15

and ethanol. The washed sample was dried and named as CDs@ANc/MoS<sub>2</sub> 12. For comparison, two other composites were also synthesized varying the mass ratio of CDs@ANc and precursors of MoS<sub>2</sub> and they are labeled as CDs@ANc/MoS<sub>2</sub> 11 and CDs@ANc/MoS<sub>2</sub> 21. **Table 1** summarizes the ratios of used reagents for the synthesis of different CDs@ANc/MoS<sub>2</sub> samples.

## 3. Results and Discussions

### 3.1. Structural and Morphological Analysis

To confirm the formation of CDs deposited ANc based MoS<sub>2</sub> nanocomposites, various spectroscopic and diffraction techniques were used.

#### 3.1.1. Spectroscopic and Structural analysis

UV-vis spectroscopy was used to measure the optical properties of CDs, as shown in Figure S2a, Supporting Information. Cigarette smoke is a complex mixture of over 5000 reported inorganic and organic substances, which was subjected to hydrothermal treatment for 12 h at 200 °C to convert them into CDs.<sup>[31]</sup> Generally, CDs show two absorption bands in their UV-Vis spectra at ≈250 and 350 nm. The UV band at about 350 nm is due to the  $n \rightarrow \pi^*$  transitions of N- or O-containing bonds at the periphery of the carbon structure, while the band around 250 nm is caused by the  $\pi \rightarrow \pi^*$  transition of aromatic C=C bonds involved in the carbon network.<sup>[33]</sup> In the present study, an absorption peak at 260 nm was observed for pure cigarette extract (diluted 11 times with distilled water), which blue shifted to 259 nm with enhanced intensity after the hydrothermal treatment, as shown in Figure S2a, Supporting Information. This increase in absorption intensity after hydrothermal treatment confirms the formation of CDs from cigarette extract.<sup>[31,34]</sup>

Fourier-transform infrared spectroscopy (FTIR)analysis was carried out to reveal the functional groups and bonding environment in the nanoclay based composites (Figure S2b, Supporting Information).An intense peak was observed at 3623 cm<sup>-1</sup> for Closite 30B which could be attributed to Si—OH bond stretching.<sup>[35]</sup> The bands at 2926 and 2853 cm<sup>-1</sup> are due to the asymmetric and symmetric stretching of the C—H bond. The Nc, ANc, and CDs@ANc exhibited characteristic bands around 1632 cm<sup>-1</sup> for H—O—H, 1472 cm<sup>-1</sup> for C—O—C, 1046 cm<sup>-1</sup> for Si—O, 918 cm<sup>-1</sup> for Al—OH, 723 cm<sup>-1</sup> for Al/Mg—OH, 625 cm<sup>-1</sup> for Al—OH, 524 cm<sup>-1</sup> for Si—O, and 471 cm<sup>-1</sup> for Si—O vibrations.<sup>[36]</sup> Further, a broad

peak at  $3383\text{ cm}^{-1}$  is due to the O—H bond stretching. Following the addition of  $\text{MoS}_2$  to CDs@ANc, noticeable peak shifts and intensity variations were observed which suggested interactions between CDs@ANc and the  $\text{MoS}_2$  (Figure S2b, Supporting Information).

Using Raman spectroscopy, more detailed insights into the structural characteristics of ANc, CDs,  $\text{MoS}_2$ , and CDs@ANc/ $\text{MoS}_2$  12 composite were explored (Figure 2a). The characteristic peak of ANc is observed at  $307\text{ cm}^{-1}$ . CDs exhibited prominent D and G bands at  $\approx 1342$  and  $\approx 1578\text{ cm}^{-1}$ , respectively. The D-band results from  $sp^3$  hybridized carbon while the G band corresponds to the presence of  $sp^2$  carbon in the CDs. CDs show an  $I_D/I_G$  ratio of 0.90, indicating a moderate degree of structural disorder.  $\text{MoS}_2$ 's characteristic Raman bands at  $\approx 353$  and  $406\text{ cm}^{-1}$  can be assigned to the  $E_{2g}$  and  $A_{1g}$  modes, respectively. The difference between these bands, i.e.,  $\Delta$ , indicates formation of multilayer or few layer  $\text{MoS}_2$ . For few layer  $\text{MoS}_2$  the value of  $\Delta$  is  $23\text{ cm}^{-1}$ , whereas for multilayer it is  $25\text{ cm}^{-1}$ . The composite CDs@ANc/ $\text{MoS}_2$  12 shows Raman bands at  $1345$  and  $1557\text{ cm}^{-1}$  due to D and G bands of CD's along with  $\text{MoS}_2$  modes at  $353$  and  $406\text{ cm}^{-1}$ . Here, the  $\Delta$  value for  $\text{MoS}_2$  bands calculated to be  $23\text{ cm}^{-1}$  indicating the formation of few layer  $\text{MoS}_2$ . The  $I_D/I_G$  ratio of CDs@ANc/ $\text{MoS}_2$  12 composite is 1.02, which demonstrates a greater no. of defects. These results confirm the coexistence of  $\text{MoS}_2$  and CDs in the composite structure.

X-ray diffraction (XRD) analysis was carried out to determine the change in crystal structure of acid treated nanoclay (ANc) and its composites. Figure 2b,c show the XRD pattern of unmodified, and modified nanoclay along with their composites. The primary XRD peak of organically modified nanoclay Closite 30B appeared at  $2\theta \approx 4.86^\circ$  corresponding to (001) plane with a  $d$ -spacing of  $1.8\text{ nm}$  (higher than naturally unmodified MMT) and a crystallite size of  $16.4\text{ nm}$ . This is due to the presence of intercalated alkylammonium molecules.<sup>[37]</sup> After the acid modification of nanoclay, the peak shifted to  $4.90^\circ$  without any reduction of crystallite size. This indicates highly stable silicate layers that do not dissociate during acid treatment. This is very crucial for the electrochemical energy storage which has been discussed further in

Section 3.2.1. When CDs were deposited onto ANc hydrothermally, a small increase in  $2\theta$  value was observed from  $4.9$  to  $5.0^\circ$  suggesting a decrease in interlayer spacing. This may be due to the partial disintegration of silicate layers or the displacement of alkylammonium molecules with small organic molecules derived from cigarette extract during hydrothermal treatment of ANc.<sup>[38,39]</sup>

To investigate the formation of ternary composite CDs@ANc/ $\text{MoS}_2$  12, XRD analysis was performed and presented in Figure 2b. The XRD peaks for pure  $\text{MoS}_2$  appeared at  $2\theta = 15.3^\circ$ ,  $33.3^\circ$ , and  $58.9^\circ$ , corresponding to (002), (100), and (110) planes, respectively (JCPDS card no. 37-1492).<sup>[40–42]</sup> The CDs@ANc/ $\text{MoS}_2$  12 nanocomposite shows a broad peak between  $4.0^\circ$  and  $16.0^\circ$ , which is absent in Nc, ANc, and CDs@ANc samples. The appearance of the broad peak may be due to the restricted growth and partial amorphous nature of  $\text{MoS}_2$  during the hydrothermal synthesis. Similar broad peak have also been reported by various research groups for the  $\text{MoS}_2$  based nanocomposites.<sup>[43–46]</sup> In addition, the intense peaks at  $2\theta$  value of  $34.2^\circ$  and  $57.0^\circ$  further confirms the formation of  $\text{MoS}_2$  in presence of CDs@ANc.

Together, these diffraction and spectroscopic investigations validate the successful synthesis of structurally stable, multicomponent nanocomposites of  $\text{MoS}_2$ , nanoclay, and CDs.

### 3.1.2. Morphological, Textural and Surface Chemical characterization

To support the XRD and Raman analysis and to further confirm the formation of nanocomposite, morphological analysis of nanoclay (Figure S3, Supporting Information) and its composites were performed using field emission scanning electron microscope (FESEM) as presented in Figure 3. From the FESEM images of ANc and Nc (Figure 3a, Figure S3, Supporting Information), no marked changes in the particle size were observed and the nanoclay sheets were intact which confirmed the stability of silicate layers during acid treatment. After the deposition of CDs on ANc, no morphological changes were observed which may be due to smaller size of CDs as depicted in Figure 3b. To confirm the deposition of CDs on ANc sheets, HRTEM analysis

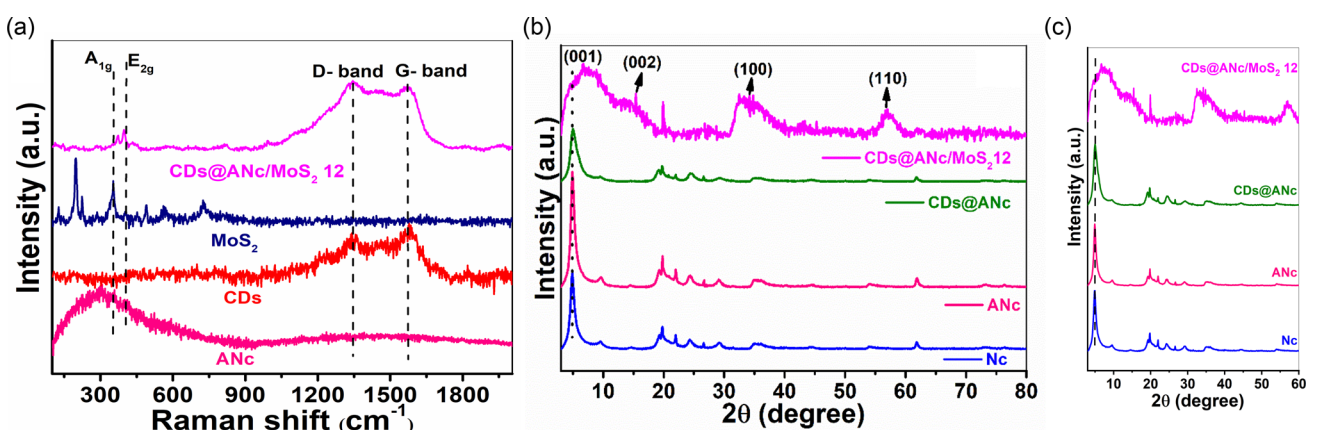


**Figure 2.** a) Raman analysis of ANc, CDs,  $\text{MoS}_2$ , and CDs@ANc/ $\text{MoS}_2$  12 composite. XRD analysis of Nc, ANc, CDs@ANc, and CDs@ANc/ $\text{MoS}_2$  12 composite: b) large  $2\theta$  range and c) small  $2\theta$  range.

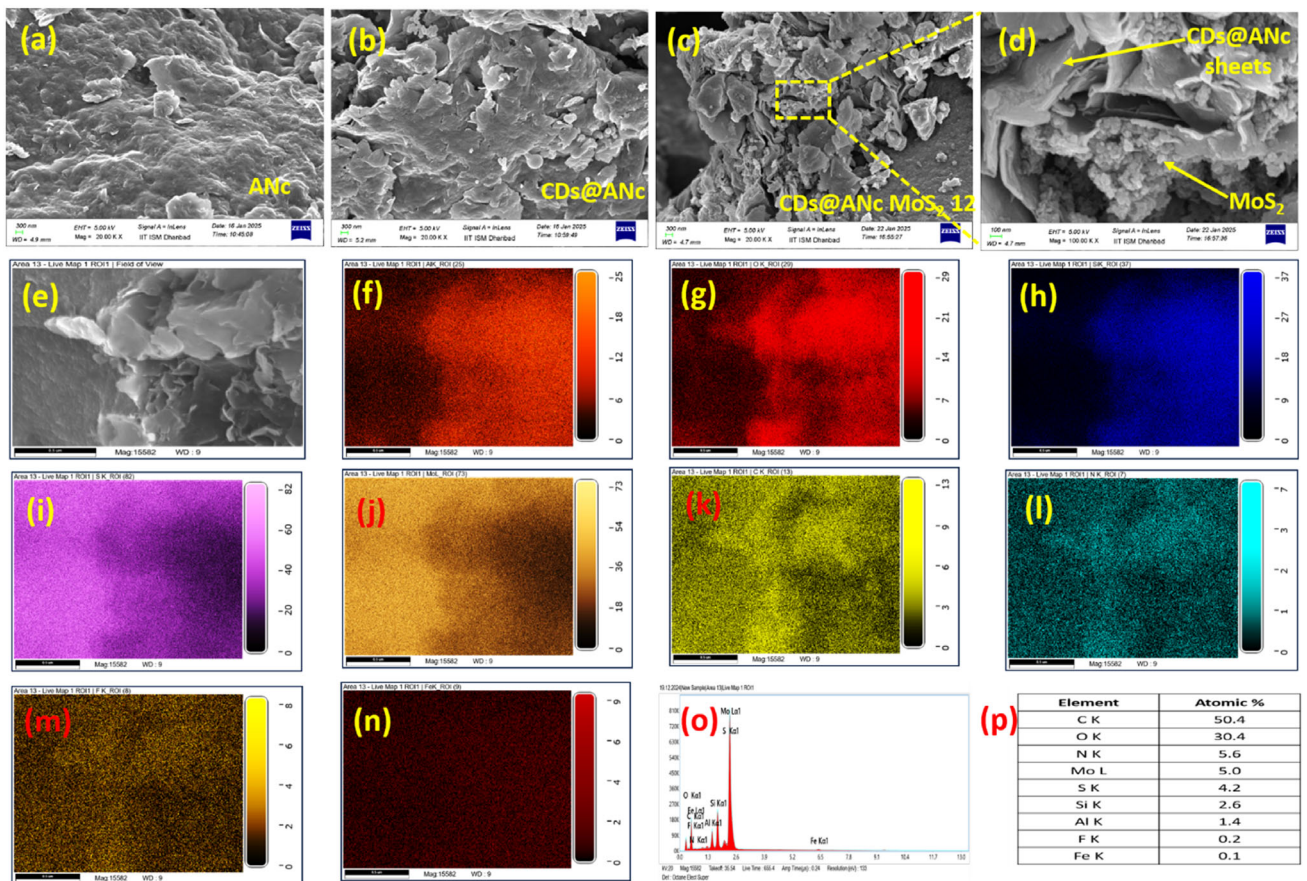


**Figure 3.** FESEM images of a) ANc and b) CDs@ANc; c) low magnification and d) high magnification; e–n) mapping of Al, O, Si, Mo, S, C, N, F, and Fe respectively; o) EDX analysis and p) atomic % of different elements of CDs@ANc/MoS<sub>2</sub> 12.

was carried out and discussed in the HRTEM section. Further, formation of MoS<sub>2</sub> in presence of CDs@ANc resulted in a sheet like morphology as shown in Figure 3c,d. The sheets are well dispersed and their distribution was further examined with energy dispersive X ray spectroscopy (EDX) mapping of a selected region of the CDs@ANc/MoS<sub>2</sub> 12 composite as shown in Figure 3e. Figure 3f–n shows the elemental distribution maps for Al, O, Si, Mo, S, C, N, F, and Fe which confirms the presence of CDs, nanoclay, and MoS<sub>2</sub>. Figure 3o,p displays the corresponding EDX analysis and atomic percentages of elements. As discussed in XRD section, broad peaks were observed for CDs@ANc/MoS<sub>2</sub> 12 which supports the deposition of MoS<sub>2</sub> over nanoclay sheets. From Raman analysis, it was observed that a multilayer MoS<sub>2</sub> formed over CDs@ANc sheets. The elemental mapping clearly shows the formation of MoS<sub>2</sub> nanosheets over the CDs@ANc substrate.

The Brunauer–Emmett–Teller (BET) N<sub>2</sub> adsorption desorption study was carried out to quantify surface area, pore volume, and pore size distribution of the ANc, CDs@ANc, and CDs@ANc/MoS<sub>2</sub> 12 composites (Figure S4, Supporting Information). The nitrogen adsorption desorption profiles (Figure S4, Supporting Information) reveal type IV isotherms with H3-type hysteresis loops, indicative of mesoporous structures. The corresponding surface area and pore size distribution data obtained from

Barrett–Joyner–Halenda (BJH) method are shown in Table S2, Supporting Information. The surface area increased by almost 4 times after the deposition of CDs on the surface of ANc. Also, the composite CDs@ANc MoS<sub>2</sub> 12 ( $56.46\text{ m}^2\text{ g}^{-1}$ ) showed more than twice the surface area compared to CDs@ANc ( $22.69\text{ m}^2\text{ g}^{-1}$ ) composite. might be due to the growth of nanosheets of MoS<sub>2</sub> between and over the ANc sheets. This well-integrated composite is advantageous to reduce the internal resistance, charge transfer resistance, and enhance the electrochemical energy storage.

In order to investigate the deposition of CDs over ANc sheets, High resolution transmission electron microscopy (HRTEM) analysis was carried out as illustrated in Figure 4a. The CDs' appear as distinct, evenly distributed nanoparticles on the surface of the clay nanosheets, indicating their deposition during the hydrothermal treatment of cigarette extract. Figure 4b represents high angle annular dark-field (HAADF) image of CDs@ANc which shows a uniform dispersion of bright spots, corresponding to CDs, across the darker nanoclay matrix. This indicates the successful deposition and good interfacial contact between the CDs and nanoclay surface. Also, the TEM EDX mapping of CDs@ANc confirms that the sheet consists of elements C, Al, N, O, Si, Mg, Fe, and F with the bright dots corresponding to that of carbon, as shown in Figure 4c–j. Figure 4k depicts the EDX data with the inset

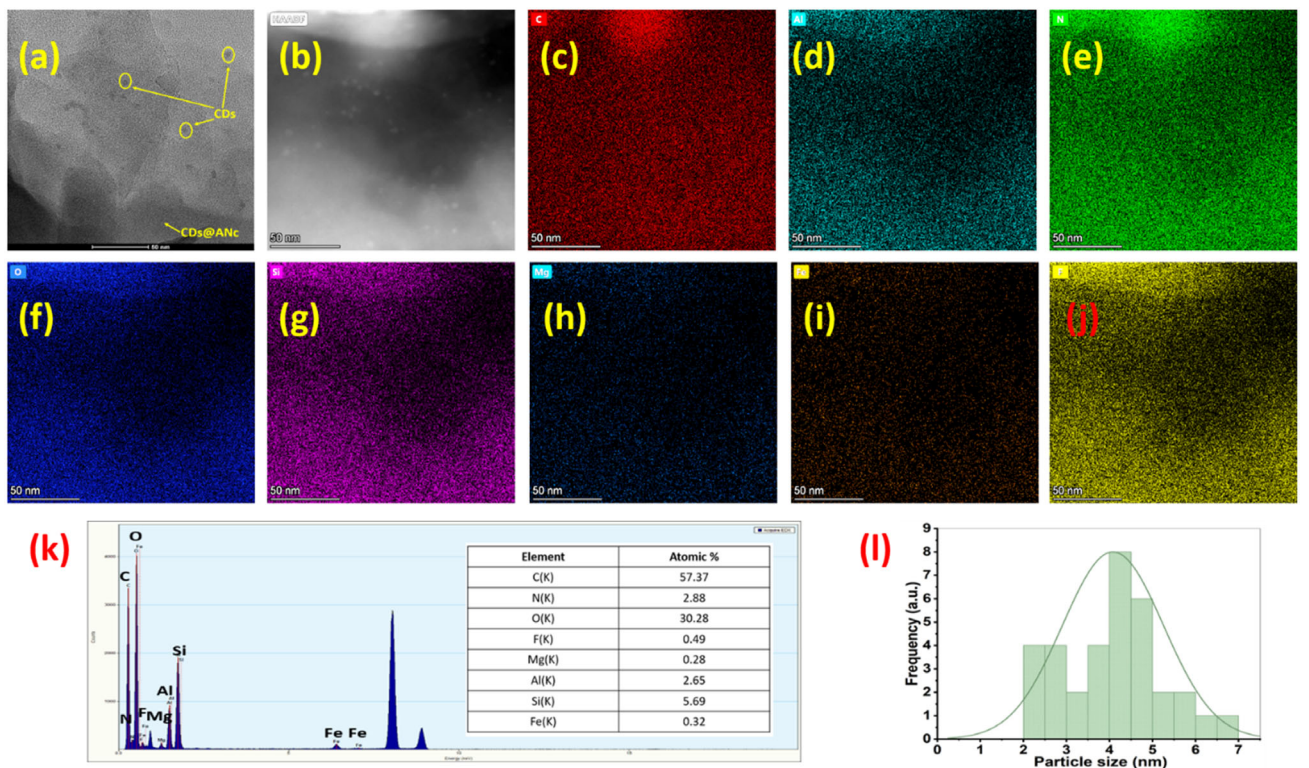


**Figure 4.** a) TEM image; b) HAADF image; c–j) TEM-EDX mapping of C, Al, N, O, Si, Mg, Fe, and F, respectively; k) EDX analysis with the inset showing atomic % of different elements of CDs@ANc; l) particle size distribution curve.

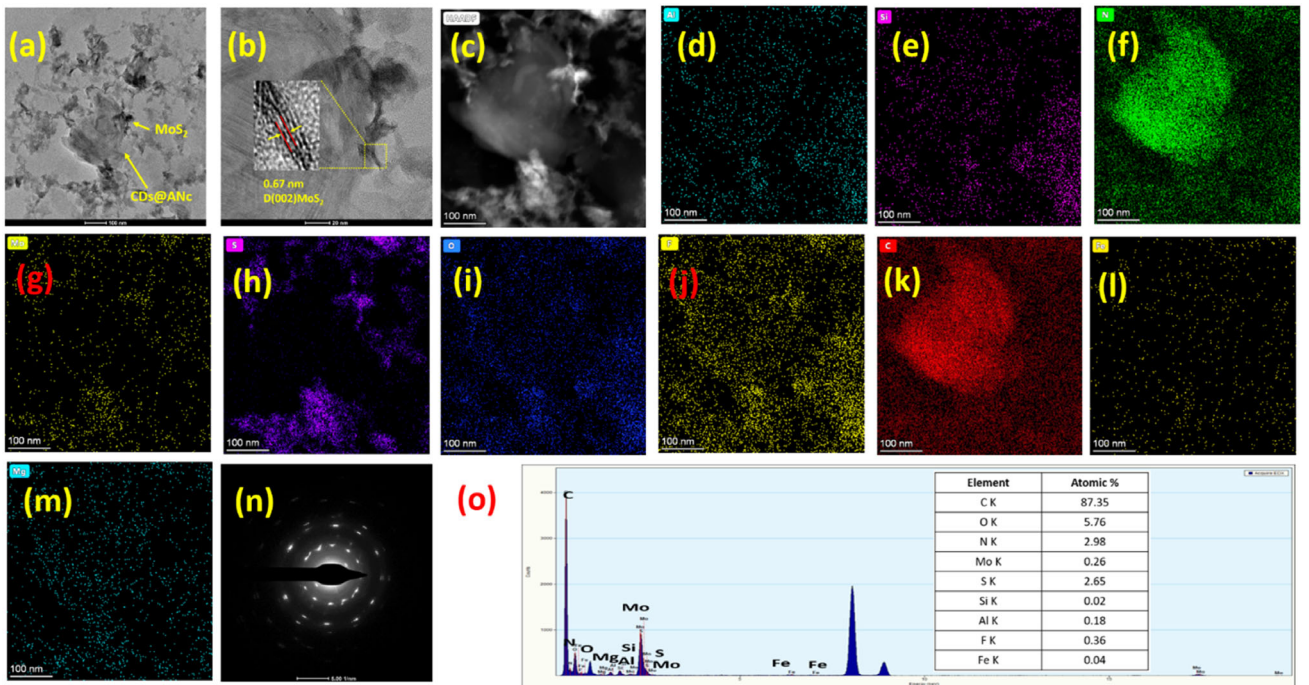


**Figure 5.** a) TEM image, b) HRTEM fringes, c) HAADF image, d–m) TEM-EDX mapping of Al, Si, N, Mo, S, O, F, C, Fe, and Mg, respectively; n) SAED pattern and o) EDX analysis with respective atomic % of CDs@ANc/MoS<sub>2</sub> 12.

showing atomic % of different elements of CDs@ANc. Figure 4l shows the histogram of particle size distribution of CDs. From Figure 4l, the average diameter of CDs was calculated to be

4.08 nm. Thus, HRTEM analysis confirms that CDs are deposited on the surfaces of ANc, and they have not intercalated within the ANc sheets.

The morphology of CDs@ANc/MoS<sub>2</sub> 12 shown in **Figure 5a** depicts MoS<sub>2</sub> nanosheets are grown over CDs@ANc sheets. The (002) plane of MoS<sub>2</sub> is shown by the HRTEM fringes in Figure 5b, with the estimated *d* spacing of 0.67 nm, characteristic of MoS<sub>2</sub>. Figure 5c represents HAADF image of CDs@ANc. Further, the formation of MoS<sub>2</sub> over CDs@ANc sheets was confirmed by TEM-EDX mapping of elements Al, Si, N, Mo, S, O, F, C, Fe, and Mg, respectively (Figure 5d-m). Moreover, the crystalline nature of MoS<sub>2</sub> is depicted in the SAED pattern, as sharp spots were obtained for CDs@ANc/MoS<sub>2</sub> 12 (Figure 5n). Figure 5o shows the corresponding EDX with the inset showing respective atomic % of CDs@ANc/MoS<sub>2</sub> 12 composite.

X-ray photoemission spectroscopy (XPS) was used to find out the oxidation states, chemical composition, and interaction among various components of CDs@ANc/MoS<sub>2</sub> 12 composite (**Figure 6**). The XPS survey scan plot of CDs@ANc/MoS<sub>2</sub> 12 (Figure 6a) confirms the presence of the elements C, S, Si, O, Al, Mo, and N along with their atomic % in Figure 6b. The Gaussian core level deconvoluted spectra of C 1s, S 2p, Si 2p, N 1s, and Mo 3d are displayed in Figure 6c-g, respectively. The deconvoluted spectra of C 1s shows three peaks at 284.6, 285.7, and 288.8 eV assigned to C=C, C—N/C—O, and C=O bonds, respectively (Figure 6c). Furthermore, for the S 2p spectra, multiple deconvoluted peaks observed as illustrated in Figure 6d. The peaks at binding energies of 161.7 and 163 eV are associated with

the 2p<sub>3/2</sub> and 2p<sub>1/2</sub> degenerate states of sulfur. These peaks correspond to the usual sulfide bond in MoS<sub>2</sub> or the S<sup>2-</sup> species in Mo—S bonds.<sup>[47]</sup> Further, the S—O bond at 169.3 eV represents oxidized sulfur species which may be formed due to the interfacial interaction and oxidative environment caused by ANc and oxygenated CDs during hydrothermal treatment.<sup>[48,49]</sup> The silicates present in Cloisite 30B show a peak at 103.4 eV (Figure 6e) due to the Si—O bond present in the silicate layers, confirming its structural integrity in the composite.<sup>[50]</sup> Three peaks in N deconvoluted spectra (Figure 6f) at 397.2, 399.5, and 402.2 eV correspond to C—N, C=N, and N—O bond, respectively. Another peak at 394.9 eV corresponds to Mo 3p<sub>3/2</sub> which overlaps with N 1s.<sup>[51-53]</sup> The deconvoluted peaks at 226, 227.2, 228.9, and 232.1 eV are visible in the Mo 3d spectra in Figure 6g which corresponds to S 2s, Mo<sup>4+</sup> 3d<sub>5/2</sub>, and Mo<sup>4+</sup> 3d<sub>3/2</sub> bonds, respectively.<sup>[54]</sup> Both the Mo 3d<sub>5/2</sub> and Mo 3d<sub>3/2</sub> spin-orbit components are represented by two different doublets in the Mo 3d XPS spectra of the MoS<sub>2</sub> sample: one at 228.8 and 231.9 eV, and another at roughly 229.9 and 233.0 eV. One doublet is ascribed to the 1T phase of MoS<sub>2</sub>, and the other associated to 2H phase.<sup>[55]</sup> Based on the area under the doublets of Mo 3d spectra of 1T and 2H phases are 61% and 39%, respectively.<sup>[55]</sup> These peaks confirm the presence of MoS<sub>2</sub> in both of its 2H and 1T phase, which enhances the electrochemical properties. Thus, the XPS study confirms the successful synthesis of CDs@ANc/MoS<sub>2</sub> 12 composite.

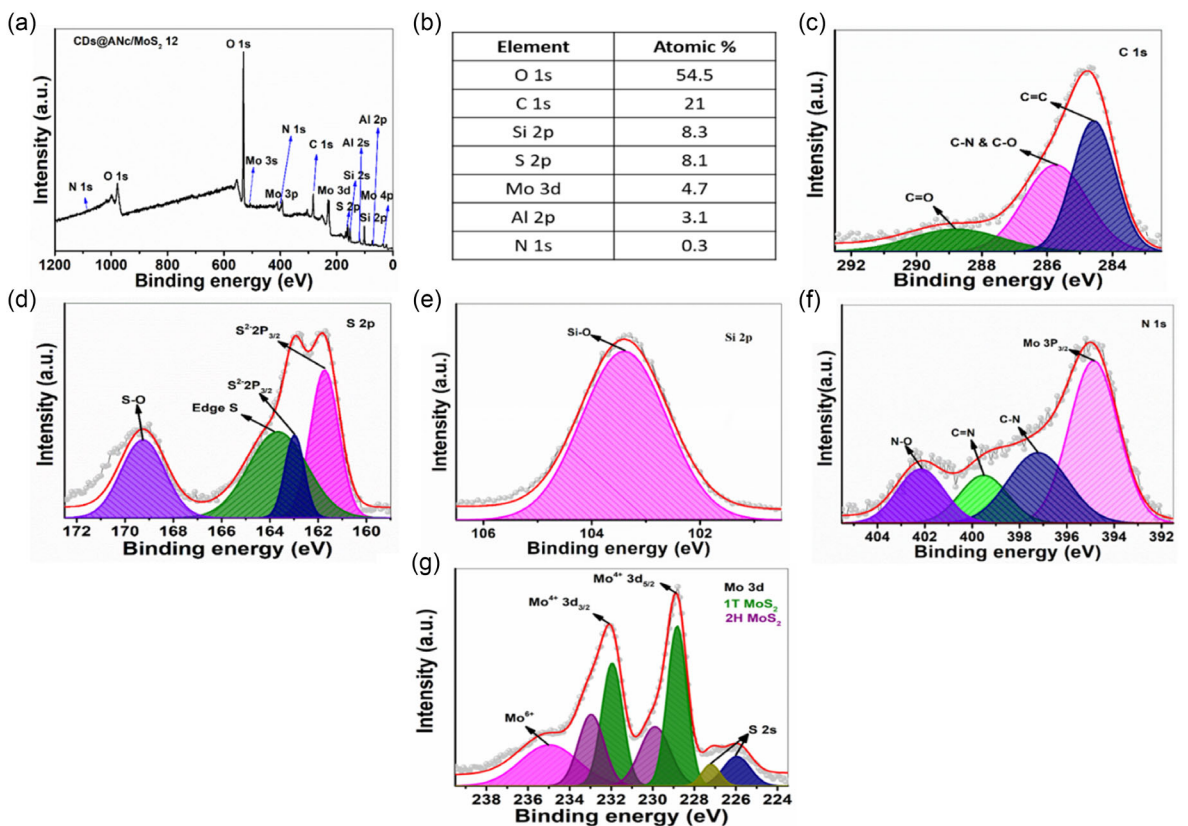


**Figure 6.** XPS analysis of CDs@ANc/MoS<sub>2</sub> 12: a) survey plot, b) atomic % of different elements present in CDs@ANc/MoS<sub>2</sub> 12; deconvoluted XPS spectra of c) C 1s, d) S 2p, e) Si 2p, f) N 1s, and g) Mo 3d for CDs@ANc/MoS<sub>2</sub> 12.

### 3.2. Electrochemical Evaluation of Synthesized Electrodes

#### 3.2.1. Three-Electrode Analysis

With the three electrode setup, the electrochemical performance (charge/discharge, capacitive characteristics, and charge transfer kinetics) of all electrodes was assessed using aqueous (aq.) 1 M Na<sub>2</sub>SO<sub>4</sub>. The electrochemical characterization techniques are discussed in Section S3.1, Supporting Information, in detail.

To optimize the different CDs@ANc composites (CDs@ANc, CDs@ANc 2.5, CDs@ANc 5, CDs@ANc 10, and CDs@ANc 30) for electrochemical energy storage, cyclic voltammetry (CV) and galvanostatic charge/discharge (GCD) analyses were carried out using three electrode setup in 1 M Na<sub>2</sub>SO<sub>4</sub> within 0–0.8 V limit. The CV analysis at various scan rates (2, 5, 10, 20, 50, 100, and 200 mV s<sup>-1</sup>) for CDs@ANc 2.5, CDs@ANc 5, CDs@ANc 10, and CDs@ANc 30 are shown in Figure S5a-d, Supporting Information, and the corresponding CV plot for CDs@ANc is shown in Figure 7a. In the CV plots, a prominent increase in CV area was observed with the increase in scan rates. This is due to the fact that as scan rate increases, the number of ions reaching the electrode electrolyte interface increases, but the charge storage mechanism may not proceed at the same rate. As a result, only a fraction of ions undergo charge transfer reactions. The ion availability at the electrode electrolyte interface contributes to a rise in measured current, thereby increasing the overall area under the CV curve at higher scan rate.<sup>[56,57]</sup> Notably, none of the electrodes exhibits redox peaks which indicates that the charge storage mechanism for different CDs@ANc composites is governed primarily by the EDLC mechanism at the electrode electrolyte interface.

To access the charge storage efficiency for different composite electrodes, a comparative CV plot at a fixed scan rate of 50 mV s<sup>-1</sup> was carried out as shown in Figure 7b. It was observed that at 50 mV s<sup>-1</sup>, CDs@ANc has the highest CV area which corresponds to maximum charge storage capacity. Further, charge discharge behaviour of as synthesized composites of CDs@ANc were also analyzed by GCD. Figure S5e-h, Supporting Information, depicts the GCD plots of CDs@ANc 2.5, CDs@ANc 5, CDs@ANc 10, and CDs@ANc 30 at different current densities (1–10 A g<sup>-1</sup>) and the corresponding GCD plot of CDs@ANc is shown in Figure 7c. The GCD comparison at 1 A g<sup>-1</sup> of all the synthesized composite electrodes reveals that CDs@ANc has highest discharge time (Figure 7d). The Sp.Cp. of all five composites, CDs@ANc 2.5, CDs@ANc 5, CDs@ANc 10, CDs@ANc, and CDs@ANc 30, at 1 A g<sup>-1</sup> was calculated to be 37, 46, 74, 86, and 33 F g<sup>-1</sup>, respectively. Thus, CDs@ANc has the highest Sp.Cp. compared to other electrodes due to better surface interaction and large number of active sites.

#### 3.2.2. Electrochemical Analysis of Fabricated Asymmetric (ASC) Device

Among all the ratios, CDs@ANc showed better performance both in CV and GCD analyses in the three electrode setup. The charge storage in this electrode follows the EDLC mechanism. So, to improve the performance, we have further incorporated pseudocapacitive MoS<sub>2</sub> into CDs@ANc in different ratios. The optimized ratio of CDs@ANc to MoS<sub>2</sub> was established by CV and GCD analyses of fabricated asymmetric devices. The composites were used as cathode and graphite as anode in 1 M

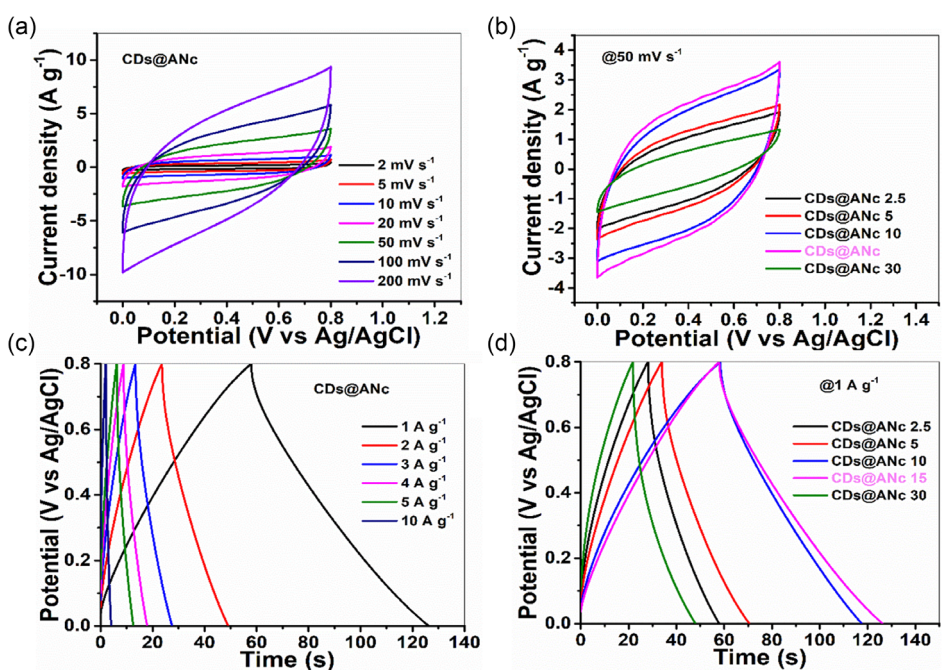


**Figure 7.** Electrochemical testing of different CDs@ANc samples using 3 electrode setup in 1 M aqueous Na<sub>2</sub>SO<sub>4</sub> throughout the potential window of 0–0.8 V: a) CV at various scan rates and c) GCD at different current densities of CDs@ANc, respectively; b) CV at fixed scan rate and d) GCD at fixed current density of different CDs@ANc samples.

TEABF<sub>4</sub>/DMSO within a potential window of 0–1.6 V. Here, DMSO was used due to its stable and higher potential window. The device fabrication process is outlined in Section S3.2, Supporting Information.

**Figure 8** depicts the CV plots recorded at 50 mV s<sup>-1</sup> and GCD measured at 1 A g<sup>-1</sup> for all the ASC devices with CDs@ANc/MoS<sub>2</sub> 21, CDs@ANc/MoS<sub>2</sub> 11, and CDs@ANc/MoS<sub>2</sub> 12 as cathode. Among all ratios, CDs@ANc/MoS<sub>2</sub> 12 exhibits a longer discharge period and a greater CV area compared to CDs@ANc/MoS<sub>2</sub> 21 and CDs@ANc/MoS<sub>2</sub> 11. The Sp.Cp. of CDs@ANc/MoS<sub>2</sub> 12 based ASC device found to be 119.7 F g<sup>-1</sup>. A summary of the Sp.Cp., energy density, and power density of all synthesized ASC devices are provided in Table S3, Supporting Information. Further, we have also compared our device performance with other reported MoS<sub>2</sub> based devices in terms of Sp.Cp., energy density, power density, cyclic stability, and capacitance retention. A comparative summary of these parameters is presented in **Table 2**.

**Figure 9a** represents the fabricated ASC device using CDs@ANc/MoS<sub>2</sub> 12 as the cathode. The CV profiles of the ASC device under various potential ranges (up to 1.6 V) at 50 mV s<sup>-1</sup> are shown in **Figure 9b**. It is apparent that even with the potential limits increased, the CV curve's characteristics remained mostly unchanged, indicating good electrochemical stability. Further, GCD at different potential window was obtained at 1 A g<sup>-1</sup> current density, and it was observed that the nature of the GCD

curve remains unaltered (**Figure 9c**). CV plots are shown at various scan rates with a 1.6 V potential limit (**Figure 9d**). The current response and the area of the CV profiles rise rapidly at higher scan rates because of the electrode surface's fast diffusion kinetics. At higher scan rate, the oxidation potential of the device shifts towards the right side, which can be due to the increasing exposure of pores on the surface, which enhances MoS<sub>2</sub> oxidation. The deviation of CV profiles from their desired rectangular shape confirms the pseudocapacitance contribution of MoS<sub>2</sub>, with distinct redox peaks at 0.9 and 0.59 V corresponding to Mo<sup>4+</sup>/Mo<sup>3+</sup> redox couple. In addition to the CDs@ANc's EDLC contribution, the redox peaks of Mo provides pseudocapacitance.

Similar to CV profiles, with the change in current densities, the nature of the GCD plots remains unchanged (**Figure 9e**). The device's Sp.Cp. within the 0 – 1.6 V potential window was ascertained using a GCD analysis, and the corresponding GCD plots is shown in **Figure 9e**. The maximum Sp.Cp. in 1 M TEABF<sub>4</sub>/DMSO electrolyte was calculated to be 119.7 F g<sup>-1</sup> and the corresponding energy density attained at 1 A g<sup>-1</sup> was 26.6 Wh kg<sup>-1</sup>. Additional factors contributing to improved electrochemical performance include better MoS<sub>2</sub> interaction and uniform growth of MoS<sub>2</sub> over the CDs@ANc sheets. One essential component for SC applications is the electrode material's stability. **Figure 9f** demonstrates the cyclic stability profile of ASC device evaluated at 5 A g<sup>-1</sup> over 12,000 cycles. The assembled device showed a

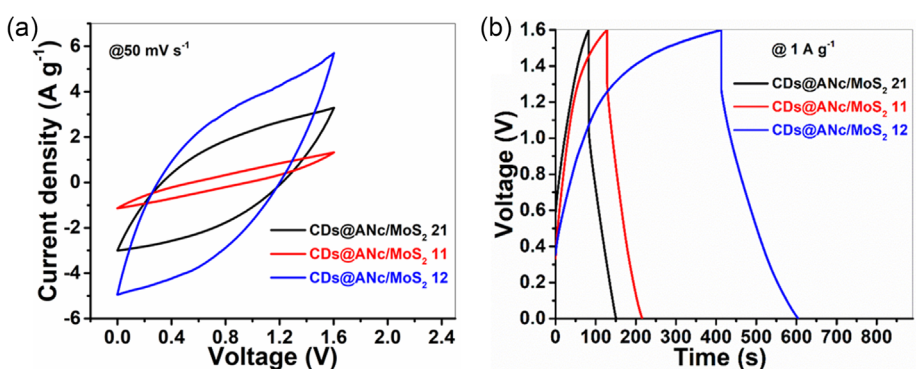


**Figure 8.** Comparative electrochemical plots of fabricated ASC devices with different CDs@ANc to MoS<sub>2</sub> ratios: a) CV at 50 mV s<sup>-1</sup> and b) GCD at 1 A g<sup>-1</sup>.

**Table 2.** Comparison of achieved Sp.Cp., energy density, power density, and capacitance retention with values reported in the literature.

Sr. no.	Sample code	Current density [A g <sup>-1</sup> ]	Sp.Cp.	Electrolyte	Energy density	Power density	Capacitance retention	Cyclic stability	References
1	HDD-MoS <sub>2</sub>	1 A g <sup>-1</sup>	68.9 F g <sup>-1</sup>	1M KOH	21.3 Wh kg <sup>-1</sup>	750 W kg <sup>-1</sup>	92%	3,000 cycles	[66]
2	MoS <sub>2</sub> -g-C <sub>3</sub> N <sub>4</sub> //AC	1 A g <sup>-1</sup>	109.3 F g <sup>-1</sup>	3 M KOH	25.6 Wh kg <sup>-1</sup>	844.9 W kg <sup>-1</sup>	92.7%	2,000 cycles	[67]
3	CMS-20-3.5	1 A g <sup>-1</sup>	102.5 F g <sup>-1</sup>	3 M KOH	36.4 Wh kg <sup>-1</sup>	800 W kg <sup>-1</sup>	87.5%	5,000 cycles	[68]
4	MSWT	0.25 A g <sup>-1</sup>	84 F g <sup>-1</sup>	1 M KCl	7.5 Wh kg <sup>-1</sup>	1.98 kW kg <sup>-1</sup>	95%	2,000 cycles	[30]
5	Ni-MoS <sub>2</sub>	1 A g <sup>-1</sup>	162 F g <sup>-1</sup>	1 M Na <sub>2</sub> SO <sub>4</sub>	9 Wh kg <sup>-1</sup>	0.5 W kg <sup>-1</sup>	60%	10,000 cycles	[69]
6	T10/MoS <sub>2</sub>	0.5 A g <sup>-1</sup>	192 F g <sup>-1</sup>	6 M KOH-PVA gel	49.2 Wh kg <sup>-1</sup>	1.3 kW kg <sup>-1</sup>	86%	1,000 cycles	[46]
7	NMS/CNT	0.5 A g <sup>-1</sup>	108 F g <sup>-1</sup>	1 M KCl	40 Wh kg <sup>-1</sup>	0.4 kW kg <sup>-1</sup>	100%	10,000 cycles	[70]
8	AC-MoS <sub>2</sub>	1 A g <sup>-1</sup>	114.2 F g <sup>-1</sup>	6 M KOH	35.7 Wh kg <sup>-1</sup>	1015 W kg <sup>-1</sup>	88.6%	10,000 cycles	[32]
9	MoS <sub>2</sub> @rGO	0.25 A g <sup>-1</sup>	81 F g <sup>-1</sup>	3M KOH	36.5 Wh kg <sup>-1</sup>	9 kW kg <sup>-1</sup>	88%	5,000cycles	[71]
10	CDs@ANc MoS <sub>2</sub> 12	1 A g <sup>-1</sup>	119.7 F g <sup>-1</sup>	1M TEABF <sub>4</sub> /DMSO	26.7 Wh kg <sup>-1</sup>	500 W kg <sup>-1</sup>	101%	12,000 cycles	This work

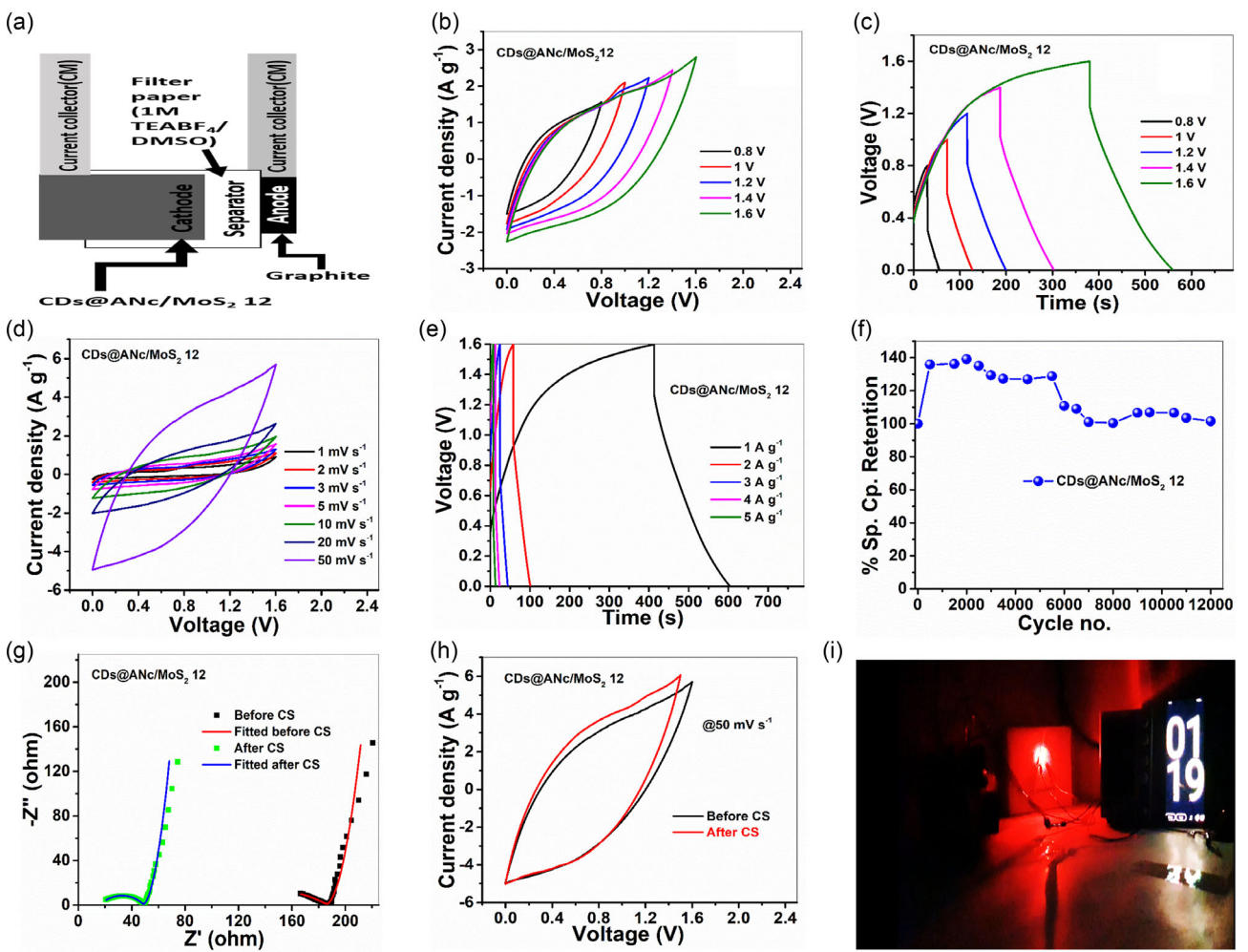


**Figure 9.** Electrochemical testing using asymmetric device: a) pictorial representation of an assembled device; b) CV and c) GCD at various potential windows, d) CV at various scan rates, e) GCD at different current densities, and f) CS plot at  $5 \text{ A g}^{-1}$ , g) impedance before and after CS, h) CV before and after CS, i) a red LED glowed after 60 s of charging of CDs@ANc/MoS<sub>2</sub> 12 based ASC device

maximum Sp.Cp. retention of almost 101%, which can be attributed to the combined contribution from 2H and 1T phases of MoS<sub>2</sub>. Initially, the capacitance increases to nearly 140% between the 500th and 5000th cycles. This is mainly due to the opening of the blocked pores by the electrolyte ions during charging and discharging cycles. Moreover, an effective pseudocapacitive redox reaction in the presence of MoS<sub>2</sub> increased the capacitance of the device initially. The lateral marginal decrease in capacitance is majorly accredited to the gradual mechanical deformation of the pseudocapacitive MoS<sub>2</sub> (2H and 1T phase) and the fractional detachments of the active materials from the current collector.<sup>[58–60]</sup> Electrochemical impedance spectroscopy (EIS) analysis was employed to examine the electroactive materials' capacitance and charge transfer behavior of CDs@ANc/MoS<sub>2</sub> 12 based ASC device (Figure 9g). The equivalent circuit fitting plots of the device before and after CS are presented in Figure S6a,b, Supporting Information. In the high frequency domain, the ohmic resistance corresponds to the contact or electrolyte resistance. The lower frequency inclination line indicates the Warburg impedance which corresponds to ion diffusion process. The charge transfer

( $R_{ct}$ ) and the solution resistance ( $R_s$ ) can be calculated from the arc's diameter and the real axis intercept, respectively. Table S4, Supporting Information, summarizes the EIS values of different composite based ASC devices. By analyzing the values of  $R_s$ , it was observed that the  $R_s$  value decreases after CS, when the MoS<sub>2</sub> loading increased in the composite electrodes. This might occur due to pseudocapacitive behavior of MoS<sub>2</sub> and fast ion diffusion. Decreased  $R_s$  value after the CS is due to the saturation of the electrodes and electrolyte's ion throughout the electrochemical process.<sup>[58]</sup> Furthermore, we contrasted the CDs@ANc/MoS<sub>2</sub> 12 CV plots measured at  $50 \text{ mV s}^{-1}$  before and after 12,000 cycles and, observed nearly identical CV area which corresponds well with the capacitance retention (Figure 9h). The CV, GCD, impedance (IMP) along with CV before and after CS of CDs@ANc MoS<sub>2</sub> 21 and CDs@ANc MoS<sub>2</sub> 11 composites are represented in Figure S7, Supporting Information.

The practical applicability of the CDs@ANc MoS<sub>2</sub> 12 composite was also ascertained by assembling six devices ( $3 \times 3 \text{ cm}$ ) in series. Following 1 min of charging [per strip (1.6 V)] for the fabricated ASC CDs@ANc MoS<sub>2</sub> 12 device, a red LED lit up for

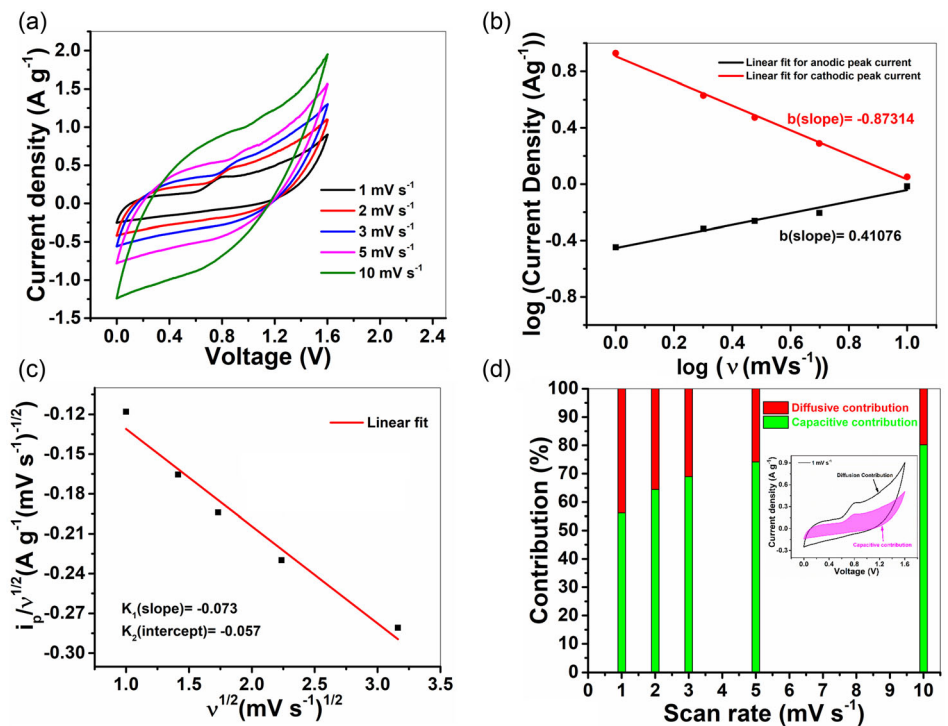


**Figure 10.** a) Slow scan rate CV plot ( $1\text{--}10 \text{ mV s}^{-1}$ ), b) plot of  $\log(v)$  versus  $\log(i)$  (current density ( $\text{A g}^{-1}$ )), c) plot of  $v^{1/2}$  versus  $i_p/v^{1/2}$ , and d) total capacitive and diffusion contribution at various scan rates (inset capacitive contribution at  $1 \text{ mV s}^{-1}$  scan rate) of CDs@ANc/MoS<sub>2</sub> 12 based ASC device.

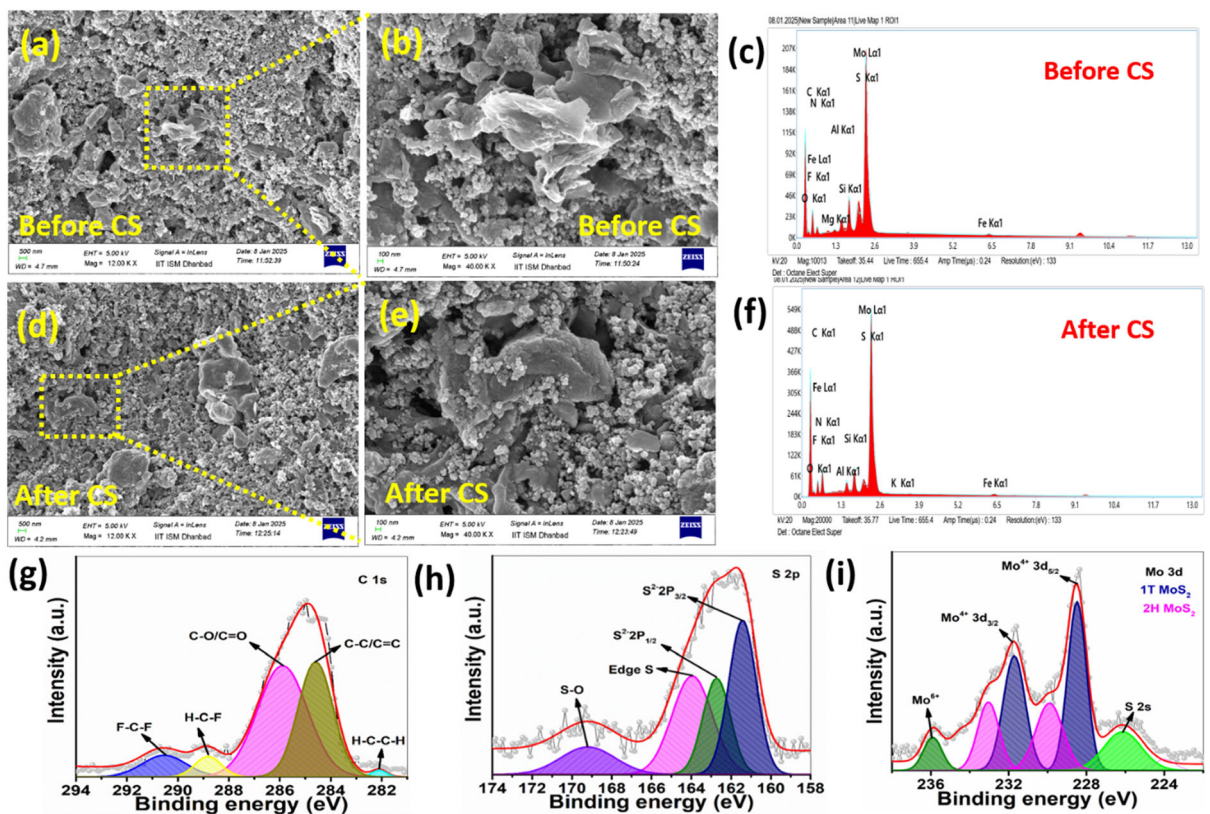


**Figure 11.** FESEM images a,d) at low magnification, b,e) at high magnification, EDX mapping c) before CS, f) after CS; XPS plot g) C 1s, h) S 2p, and i) Mo 3d of CDs@ANc/MoS<sub>2</sub> 12.

2 min 30 s (Figure 9i, Supporting video V2, Supporting Information). Furthermore, assembled ASC devices were recharged for 1 min and able to glow a multicolored disco LED for 50 s (Figure S8, Supporting Information) (Supporting video V3, Supporting Information).

To understand the kinetics of charge storage, CV at lower scan rates was performed and shown in Figure 10a. Using the power law (Equation 1),<sup>[61]</sup> the  $b$  (slope) value was calculated to be 0.87 for cathodic peak current as shown in Figure 10b, suggesting a transition controlled reaction.<sup>[62,63]</sup> Furthermore, to examine the percentage contribution, the Dunn (Equation 2)<sup>[63]</sup> method was used. From the  $v^{1/2}$  versus  $i_p/v^{1/2}$  plot (Figure 10c),<sup>[64,65]</sup> the capacitive ( $K_1 v$ ) and diffusion ( $K_2 v^{1/2}$ ) contribution was calculated and found to be 56.15% (capacitive) and 43.85% (diffusion) (Figure 10d).

$$i_p = av^b \text{ or } \log i_p = \log a + b \log v \quad (1)$$

where  $v$  is the scan rate,  $i_p$  is the peak current, and  $a, b$  are the fitting parameters.

$$i_p = K_1 v + K_2 v^{1/2} \quad (2)$$

FESEM analysis was performed for the cathode material before and after cyclic stability at different magnification ranges (Figure 11a,b,d,e) to evaluate the morphological changes. Figure 11 did not show any such changes in the active material morphology. The elemental compositions were validated by EDS analysis of electrodes before and after CS (Figure 11c,f). After 12,000 cycles, the powder diffraction results of CDs@ANc/MoS<sub>2</sub> 12 revealed that the major diffraction peak positions are well matched with as synthesized materials (Figure S9, Supporting Information). Comparative XPS analysis before and after cyclic stability (12,000 cycles) suggested unchanged binding energy peak position values for Mo 3d (S 2s, Mo<sup>4+</sup> 3d<sub>5/2</sub>, Mo<sup>4+</sup> 3d<sub>3/2</sub>, and Mo<sup>6+</sup>), S 2p (S<sup>2-</sup> 2p<sub>3/2</sub>, S<sup>2-</sup> 2p<sub>1/2</sub>, and S—O), and C 1s (C—C/C=C, O—C/C=O), which confirms the electrode material is electrochemically stable (Figure 11g-i). Additionally, C—F bond is present in the C 1s spectra due to the presence of polyvinylidene fluoride binder (PVDF) used for making the slurry of electrode material.

## 4. Conclusion

In summary, a simple hydrothermal process was employed to synthesize CDs from cigarette smok extract, which was subsequently used to enhance the surface conductivity of Closite 30B. The enhanced electrochemical performance of nanoclay in presence of CDs was demonstrated by various electrochemical analysis. Incorporation of MoS<sub>2</sub> further boosted the electrochemical energy storage capacity of CDs@ANc/MoS<sub>2</sub> 12 because of the efficient combination of pseudocapacitive type MoS<sub>2</sub> and EDLC type CDs deposited nanoclay. The ASC device assembled with CDs@ANc/MoS<sub>2</sub> 12 as cathode and graphite as anode exhibited a Sp.Cp. of 119.7 F g<sup>-1</sup> with an energy density of 26.6 W h kg<sup>-1</sup> and  $\approx$ 101% retention of Sp.Cp. after 12,000 GCD cycles.

The improved electrochemical activities of CDs@ANc/MoS<sub>2</sub> 12 attributed to uniform growth of MoS<sub>2</sub> on the surface of CDs@ANc, facile ion diffusion, large surface area, and abundant active sites owing to the presence of CDs. Overall, this strategy demonstrates an ecofriendly and low cost approach for fabricating high performance energy storage devices by upcycling hazardous cigarette smoke, and utilizing closite 30B nanoclay, thereby addressing both environmental pollution and energy demand challenges.

## Acknowledgements

The IIT (ISM), Dhanbad is acknowledged by Khusboo Kumari for the SRF fellowship and providing research facilities. The IIT (ISM), Dhanbad is acknowledged by Arif Ali for the IPDF fellowship (DAR/IPDF/CCB/53/2023).

## Conflicts of Interest

The authors declare no conflict of interest.

## Author Contributions

**Khusboo Kumari:** writing—original draft, methodology, investigation, data curation, conceptualization. **Arif Ali:** writing—review and editing, investigation, data curation. **Sourav Acharya:** visualization, formal analysis. **Chandan Kumar Maity:** writing—review and editing, visualization, formal analysis. **Ganesh Chandra Nayak:** writing—review and editing, visualization, supervision, funding acquisition, conceptualization.

## Data Availability Statement

The data that support the findings of this study are available from the corresponding author upon reasonable request.

**Keywords:** asymmetric supercapacitor • carbon dots • cigarette smoke • MoS<sub>2</sub> • nanoclay

- [1] Z. Abdouleh, A. Gastli, L. Ben-Brahim, M. Haouari, N. A. Al-Emadi, *Renew. Energy* **2017**, *113*, 266.
- [2] S. Mubarak, D. Dhamodharan, P. N. P. Ghoderao, H.-S. Byun, *Coord. Chem. Rev.* **2022**, *471*, 214741.
- [3] C. Xu, B. Xu, Y. Gu, Z. Xiong, J. Sun, X. S. Zhao, *Energy Environ. Sci.* **2013**, *6*, 1388.
- [4] P. Simon, Y. Gogotsi, *Nat. Mater.* **2008**, *7*, 845.
- [5] G. Wang, L. Zhang, J. Zhang, *Chem. Soc. Rev.* **2012**, *41*, 797.
- [6] T. Ramachandran, S. S. Sana, K. D. Kumar, Y. A. Kumar, H. H. Hegazy, S. C. Kim, *J. Energy Storage* **2023**, *73*, 109096.
- [7] C. K. Maity, N. Goswami, K. Verma, S. Sahoo, G. C. Nayak, *J. Energy Storage* **2020**, *32*, 101993.
- [8] S.-J. Wen, X.-T. Yin, L. Nazar, *Act. Passiv. Electron. Components* **1994**, *16*, 145.
- [9] M.-S. Chen, W. Fu, Y. Hu, M.-Y. Chen, Y.-J. Chiou, H.-M. Lin, M. Zhang, Z. Shen, *Nanoscale* **2020**, *12*, 16262.

- [10] R. Oraon, A. De Adhikari, S. K. Tiwari, G. C. Nayak, *ACS Sustain. Chem. Eng.* **2016**, *4*, 1392.
- [11] S. Ummartyotin, N. Bunnak, H. A. Manuspiya, *Renew. Sustain. Energy Rev.* **2016**, *61*, 466.
- [12] J. H. Jia, X. F. Lu, C. C. Yang, Q. Jiang, *J. Mater. Chem. A.* **2024**, *12*, 1359.
- [13] T. Akram, L. Arshad, T. Ahmed, A. Saleem, M. Ammar, A. Yusaf, *Mater. Sci. Eng. B* **2024**, *299*, 117002.
- [14] S. S. Rifah, M. S. Zaman, A. A. Piya, S. U. D. Shamim, *Phys. Chem. Chem. Phys.* **2024**, *26*, 6667.
- [15] M. Habib, Z. Muhammad, Y. A. Haleem, S. Farooq, R. Nawaz, A. Khalil, F. Shaheen, H. Naeem, S. Ullah, R. Khan, *Mater. Adv.* **2024**, *5*, 1088.
- [16] Y. Wu, M. Sun, *Nanoscale Horizons* **2024**, *9*, 215.
- [17] T. Akram, L. Arshad, T. Ahmed, A. Saleem, M. Ammar, A. Yusaf, *Mater. Sci. Eng. B* **2024**, *299*, 117002.
- [18] V. K. Soni, T. Roy, S. Dhara, G. Choudhary, P. R. Sharma, R. K. Sharma, *J. Mater. Sci.* **2018**, *53*, 10095.
- [19] B. S. Chikkatti, A. M. Sajjan, N. R. Banapurmath, J. K. Bhutto, R. Verma, T. M. Yunus Khan, *Polymers* **2023**, *15*, 4587.
- [20] S. Timakwe, S. Ngcobo, R. Smith, M. N. Matoetoe, *Front. Sensors* **2024**, *5*, 1395853.
- [21] A. Inayat, K. Albalawi, A. Rehman, S. Adnan, Y. A., E. A. M. Saleh, M. A. Alamri, A. A. El-Zahhar, A. Haider, S. M. Abbas, *Mater. Today Commun.* **2023**, *34*, 105479.
- [22] V. C. Hoang, V. G. Gomes, *Mater. Today Energy* **2019**, *12*, 198.
- [23] F. A. Permatasari, M. A. Irham, S. Z. Bisri, F. Iskandar, *Nanomaterials* **2021**, *11*, 91.
- [24] J. Yan, S. Li, B. Lan, Y. Wu, P. S. Lee, *Adv. Funct. Mater.* **2020**, *30*, 1902564.
- [25] L. Kang, S. Liu, Q. Zhang, J. Zou, J. Ai, D. Qiao, W. Zhong, Y. Liu, S. C. Jun, Y. Yamauchi, J. Zhang, *ACS Nano* **2024**, *18*, 2149.
- [26] H. Huang, Y. Cui, Q. Li, C. Dun, W. Zhou, W. Huang, L. Chen, C. A. Hewitt, D. L. Carroll, *Nano Energy* **2016**, *26*, 172.
- [27] A. P. Nayak, S. Bhattacharyya, J. Zhu, J. Liu, X. Wu, T. Pandey, C. Jin, A. K. Singh, D. Akinwande, J.-F. Lin, *Nat. Commun.* **2014**, *5*, 3731.
- [28] X. Geng, Y. Zhang, Y. Han, J. Li, L. Yang, M. Benamara, L. Chen, H. Zhu, *Nano Lett.* **2017**, *17*, 1825.
- [29] W. Choi, N. Choudhary, G. H. Han, J. Park, D. Akinwande, Y. H. Lee, *Mater. Today* **2017**, *20*, 116.
- [30] S. Kumar, M. Bulla, S. Sindhu, R. Devi, A. K. Mishra, V. Kumar, *Vacuum* **2025**, *238*, 114265.
- [31] C. K. Maity, S. De, A. Panigrahi, S. Acharya, K. Verma, M. J. Kim, G. C. Nayak, *Compos. Part B Eng.* **2023**, *264*, 110887.
- [32] R. K. Abuelela, S. S. Mahmoud, M. M. Ahmed, Y. F. Barakat, S. G. Mohamed, *Fuel* **2025**, *401*, 135925.
- [33] H. Miao, Y. Wang, X. Yang, *Nanoscale* **2018**, *10*, 8139.
- [34] C. K. Maity, S. Acharya, S. De, S. K. Tiwari, K. Kumari, A. Joy, S. Sahoo, S. Sahoo, G. C. Nayak, *J. Energy Storage* **2024**, *102*, 114099.
- [35] S. Sharma, M. Kumar Poddar, V. S. Moholkar, *Ultrason. Sonochem.* **2017**, *36*, 212.
- [36] E. Günister, D. Pestrelj, C. H. Ünlü, O. Atıcı, N. Güngör, *Carbohydr. Polym.* **2007**, *67*, 358.
- [37] N. H. Tran, G. R. Dennis, A. S. Milev, G. S. K. Kannangara, P. Williams, M. A. Wilson, R. N. Lamb, *J. Colloid Interface Sci.* **2006**, *297*, 541.
- [38] R. C. Walters, E. H. Fini, T. Abu-Lebdeh, *Am. J. Eng. Appl. Sci.* **2014**, *7*, 66.
- [39] M. Ansari, A. Aroujalian, A. Raisi, B. Dabir, M. Fathizadeh, *Adv. Powder Technol.* **2014**, *25*, 722.
- [40] C. P. Veeramalai, F. Li, Y. Liu, Z. Xu, T. Guo, T. W. Kim, *Appl. Surf. Sci.* **2016**, *389*, 1017.
- [41] Y. Wang, E. Della Gaspera, B. J. Carey, P. Atkin, K. J. Berean, R. M. Clark, I. S. Cole, Z.-Q. Xu, Y. Zhang, Q. Bao, J. Z. Ou, T. Daeneke, K. Kalantar-zadeh, *Nanoscale* **2016**, *8*, 12258.
- [42] Q. Wang, J. Li, *J. Phys. Chem. C.* **2007**, *111*, 1675.
- [43] Y. Zhang, Q. Jia, M. Ma, W. Wang, B. Li, X. Wang, Y. Zhang, X. Zhu, *Mater. Today Chem.* **2025**, *43*, 102477.
- [44] P. Naveenkumar, J. Yesuraj, M. Maniyazagan, H.-W. Yang, K. Kim, S.-J. Kim, *J. Alloys Compd.* **2025**, *1014*, 178737.
- [45] M. Kumar, R. Yousofi, A. Vasistha, G. K. Yogesh, S. K. Sharma, K. Yadav, C. Devi, *J. Mater. Sci. Mater. Electron.* **2025**, *36*, 1026.
- [46] V. Shrivastav, D. Mansi, P. Shrivastav, V. Kaur, A. Hołdyski, M. Krawczyńska, A. Tiwari, K. U., A. Deep, W. Nogala, S. Sundriyal, *Sci. Rep.* **2023**, *13*, 20675.
- [47] A. Santoni, F. Rondino, C. Malerba, M. Valentini, A. Mittiga, *Appl. Surf. Sci.* **2017**, *392*, 795.
- [48] Y. K. Sonia, M. K. Paliwal, S. K. Meher, *Sustain. Energy Fuels* **2021**, *5*, 973.
- [49] X. Chen, Z. Ding, H. Yu, H. Ge, W. Liu, S. Sun, *Mater. Chem. Front.* **2021**, *5*, 7606.
- [50] Z. Li, H. Zhao, P. Lv, Z. Zhang, Y. Zhang, Z. Du, Y. Teng, L. Zhao, Z. Zhu, *Adv. Funct. Mater.* **2018**, *28*, 1605711.
- [51] J. Liu, S. Tang, Y. Lu, G. Cai, S. Liang, W. Wang, X. Chen, *Energy Environ. Sci.* **2013**, *6*, 2691.
- [52] Y. Zeng, X. Zeng, S. Wang, Y. Hu, W. Wang, S. Yin, T. Ren, Y. Zeng, J. Lu, Z. Guo, Y. Xiao, W. Jin, *Nanotechnology* **2020**, *31*, 015702.
- [53] C. Wu, D. Liu, H. Li, J. Li, *Small* **2018**, *14*, 1704227.
- [54] H. Fan, R. Wu, H. Liu, X. Yang, Y. Sun, C. Chen, *J. Mater. Sci.* **2018**, *53*, 10302.
- [55] M. Shrivastav, V. Kumar, K. Rana, R. Dhiman, *J. Appl. Electrochem.* **2024**, *54*, 1517.
- [56] K. R. Cooper, M. Smith, *J. Power Sources* **2006**, *160*, 1088.
- [57] K. Kumari, A. Joy, P. Saren, S. Acharya, S. De, A. K. Behera, B. Mahanti, G. Chandra Nayak, *Mater. Chem. Phys.* **2024**, *313*, 128677.
- [58] M. Moniruzzaman, C. K. Maity, S. De, M. J. Kim, J. Kim, *ACS Appl. Nano Mater.* **2024**, *7*, 6636.
- [59] C. K. Maity, M. Kim, M. J. Kim, *J. Alloys Compd.* **2025**, *1031*, 181109.
- [60] S. Sahoo, A. Milton, A. Sood, R. Kumar, S. Choi, C. K. Maity, S. S. Han, *J. Energy Storage* **2024**, *99*, 113321.
- [61] W. Basree, A. Ali, N. Khan, M. Z. Khan, G. C. Nayak, K. A. Siddiqui, M. Ahmad, *Mater. Adv.* **2024**, *5*, 8265.
- [62] M. Z. Iqbal, S. S. Haider, S. Siddique, M. R. A. Karim, S. Zakar, M. Tayyab, M. M. Faisal, M. Sulman, A. Khan, M. Baghayeri, M. A. Kamran, T. Alherbi, M. J. Iqbal, T. Hussain, *J. Energy Storage* **2020**, *27*, 101056.
- [63] S. Pervez, M. Z. Iqbal, *Small* **2023**, *19*, 2305059.
- [64] C. Luo, G. Xu, X. Ji, S. Hou, L. Chen, F. Wang, J. Jiang, Z. Chen, Y. Ren, K. Amine, C. Wang, *Angew. Chem. Int. Ed.* **2018**, *57*, 2879.
- [65] H. Sun, X. Li, K. Jin, X. Lai, J. Du, *Nanoscale Adv.* **2022**, *4*, 1422.
- [66] N. Joseph, P. Muhammed Shafi, A. Chandra Bose, *New J. Chem.* **2018**, *42*, 12082.
- [67] S. Suganya, G. Janani, M. Aparna, S. Sambasivam, K. Yusuf, F. Ran, S. Sudhahar, *Electrochim. Acta* **2025**, *513*, 145595.
- [68] C. Liu, P. Yang, X. Zhang, *Int. J. Hydrogen Energy* **2025**, *97*, 1348.
- [69] S. J. Panchu, K. Raju, P. Singh, D. D. Johnson, H. C. Swart, *ACS Appl. Energy Mater.* **2023**, *6*, 2187.
- [70] X. Yang, L. Zhao, J. Lian, *J. Power Sources* **2017**, *343*, 373.
- [71] H. Sun, H. Liu, Z. Hou, R. Zhou, X. Liu, J.-G. Wang, *Chem. Eng. J.* **2020**, *387*, 124204.

Manuscript received: June 2, 2025

Revised manuscript received: August 10, 2025

Version of record online: